Journal of Materials Chemistry A

ROYAL SOCIETY OF CHEMISTRY

PAPER

View Article Online
View Journal | View Issue

Cite this: J. Mater. Chem. A, 2022, 10, 14392

Liquid-phase synthesis of the $Li_{10}GeP_2S_{12}$-type phase in the Li–Si–P–S–Cl system†

Tomohiro Ito, [ab] Satoshi Hori,[c] Masaaki Hirayama[bc] and Ryoji Kanno*[c]

The $Li_{10}GeP_2S_{12}$-type phase in the Li–Si–P–S–Cl system (LSiPSCl) shows the highest lithium ionic conductivity among the Li ion conductors reported to date. With the aim of establishing a large-scale production process for LSiPSCl, we report the development of a liquid-phase approach to its synthesis. The ionic conductivity and particle morphology are characterised, and their effects on the electrochemical properties of the LSiPSCl phase synthesised by the new liquid-phase method (L-LSiPSCl) are investigated. An L-LSiPSCl phase with an ionic conductivity of 6.6 mS cm^{-1} at 298 K is obtained by adjusting the sulfur ratio in the dissolved starting materials. Compared with the LSiPSCl phase synthesised *via* the conventional solid-state approach (S-LSiPSCl), L-LSiPSCl shows an increased grain-boundary resistivity and its particles consisted of small porous grains. An all-solid-state cell prepared using L-LSiPSCl as the solid electrolyte exhibits stable cycling, with a discharge capacity retention of >97% after 100 cycles; this is a comparable performance to that of the S-LSiPSCl-based reference cell, indicating that L-LSiPSCl functions stably as a solid electrolyte in all-solid-state batteries. Finally, this study suggests that liquid-phase synthesis is a promising approach for the large-scale production of sulfides that exhibit high ionic conductivities, such as LSiPSCl.

Received 8th April 2022
Accepted 25th May 2022

DOI: 10.1039/d2ta02834d

rsc.li/materials-a

Introduction

All-solid-state lithium batteries promise an improved safety profile and reduced flammability compared to conventional lithium-ion batteries due to the fact that they employ less-flammable solid electrolytes instead of flammable organic electrolytes.[1] These solid electrolytes, such as oxides, sulfides, hydrides, halides, and polymers,[2] are key to improving the performances of all-solid-state lithium batteries, wherein sulfide solid electrolytes with high ionic conductivities have attracted particular attention. More specifically, a high ionic conductivity can impart all-solid-state batteries with higher power densities than conventional lithium-ion batteries.[3,4] For example, $Li_{10}GeP_2S_{12}$ (LGPS) is a conductive sulfide with an especially high ionic conductivity, exceeding 10 mS cm^{-1} at 300 K.[5] This high conductivity is related to its unique crystal structure (*i.e.*, the LGPS-type structure), which is shown in Fig. S1.† In the LGPS crystal, one-dimensional (1D) chains, which are formed from LiS_6 octahedra and $[Ge/P]S_4$ tetrahedra with a common edge, are connected by PS_4 tetrahedra with a common corner. These polyhedral structural units comprise a framework inside which Li ions are widely distributed along the *c*-axis. In previous studies, the substitution of cations and anions has been applied to LGPS to synthesise a wide variety of solid electrolytes with LGPS-type structures possessing different properties. For example, $Li_{9.54}Si_{1.74}P_{1.44}S_{11.7}Cl_{0.3}$ (LGPS-type phase in the Li–Si–P–S–Cl system: LSiPSCl), in which Ge and S are substituted by Si and Cl, respectively, exhibits the highest ionic conductivity among the various lithium-ion conductors reported to date (*i.e.*, 25 mS cm^{-1} at 298 K).[6] In addition to its ionic conductivity, the electrochemical[7–9] and atmospheric stabilities[10,11] of LGPS were also improved following chemical substitution.

The high-yielding and high-purity large-scale production of LGPS-type solid electrolytes must also be considered to permit the commercialisation of such all-solid-state batteries. However, LGPS-type solid electrolytes are conventionally synthesised *via* a solid-state method based on mechanical mixing and milling, which requires significant amounts of energy and typically provides low yields. Liquid-phase syntheses are therefore expected to be an alternative method for large-scale production, and to date, they have been applied to synthesising various sulfide-based solid electrolytes.[12] In liquid-phase synthesis, the particle shape and size of the raw materials can be controlled by their dissolution in a solvent without the requirement for milling. While many liquid-phase synthetic

[a]Mitsubishi Gas Chemical Company, Inc., Mitsubishi Building 5-2, Marunouchi 2-chome Chiyoda-ku, Tokyo 100-8324, Japan
[b]Department of Chemical Science and Engineering, School of Materials and Chemical Technology, Tokyo Institute of Technology, 4259 Nagatsuta, Midori, Yokohama 226-8502, Japan
[c]Research Center for All-Solid-State Battery, Institute of Innovative Research (IIR), Tokyo Institute of Technology, 4259 Nagatsuta, Midori, Yokohama 226-8502, Japan. E-mail: kanno@echem.titech.ac.jp

† Electronic supplementary information (ESI) available. See https://doi.org/10.1039/d2ta02834d

routes have been reported for solid electrolytes in the Li–P–S system,[13–15] only a few reports describe the liquid-phase synthesis of LGPS-type solid electrolytes, such as the preparation of germanium-containing electrolytes using hydrazine,[16] methanol,[17] and ethanol–tetrahydrofuran[18] as solvents. Moreover, the liquid-phase method has yet to be successfully applied to LSiPSCl, despite the fact that this phase is known to exhibit an extremely high ionic conductivity.

Thus, we herein report the development of a liquid-phase method for the preparation of LGPS-type LSiPSCl. The physical and electrochemical properties of the resulting LSiPSCl (*i.e.*, L-LSiPSCl) are characterised and compared with those of its counterpart system prepared *via* the conventional solid-state mechanical mixing approach (*i.e.*, S-LSiPSCl). Finally, the crystal structure, ionic conductivity, and particle morphology are examined, and the influences of these factors on the electrochemical properties of L-LSiPSCl are revealed.

Experimental

Liquid-phase synthesis of LSiPSCl

The starting materials used for the synthesis were Li_2S (>99.98%, Sigma-Aldrich), SiS_2 (>99.999%, Hangzhou Ocean Chemical Co., Ltd, China), P_2S_5 (>99%, Sigma-Aldrich), and LiCl (>99%, Kojundo Chemical Laboratory Co., Ltd, Japan). These starting materials were weighed to yield a nominal elemental molar ratio of $Li_{10.02}Si_{1.47}P_{1.56}S_{11.7}Cl_{0.3}$, where we obtained reasonably phase-pure samples in both liquid-phase and solid-state methods. This nominal composition is slightly different from the previously reported composition for LSiPSCl (*i.e.*, $Li_{9.54}Si_{1.74}P_{1.44}S_{11.7}Cl_{0.3}$), probably due to the different starting materials used in synthesis. The starting materials were added to anhydrous acetonitrile (ACN; >99.8%, FUJIFILM Wako Pure Chemical Corporation, Japan), as described below.

Preparation of the homogeneous solution containing Li, P, and S. Li_2S (1.326 g) and P_2S_5 (6.415 g) were mixed in ACN (90 mL) and stirred for 3 h at 298 K to provide a homogeneous solution, denoted as the homogeneous Li–P–S solution.

Preparation of the homogeneous solution containing Li, Si, and S. Li_2S (1.250 g), SiS_2 (5.016 g), and S (0.0, 0.878, 2.527 g) were mixed with ACN (220 mL) and stirred for 120 h at 298 K. After this time, some of the raw materials remained as a suspension, and so the obtained solution was filtered using a membrane filter (hydrophilic PTFE membrane, 0.1 μm pore size). The amount of residual powder adhering to the membrane filter was too small to affect the composition of the resultant filtrate, which was a homogeneous solution containing Li, Si, and S. The solution obtained in this step was denoted as the homogeneous Li–Si–S solution.

Preparation of the precursor slurry solution. Following mixing of the homogeneous solutions obtained in the previous two steps, LiCl (0.471 g) was added, and the resulting suspension was stirred for 3 h at 298 K to give a homogeneous solution. Subsequently, fine-Li_2S (5.687 g) was added to the homogeneous solution and stirred for 1 h at 298 K to obtain the precursor slurry solution. The fine-Li_2S required for this step was prepared by wet milling the as-purchased Li_2S powder in anhydrous heptane (>99%, FUJIFILM Wako Pure Chemical Corporation, Japan) using a planetary ball mill (Pulverisette 7 Classic Line, Fritsch, Germany) at a rotation speed of 300 rpm for 20 h and then drying the obtained suspension at 453 K for 3 h under vacuum.

Drying and sintering to yield L-LSiPSCl. The precursor slurry solution was dried at 453 K for 3 h under vacuum to remove all of the solvent and obtain the precursor powder. Finally, the precursor powder was sintered by heating at 748 K for 8 h under a flow of Ar gas to obtain the final L-LSiPSCl product.

Solid-state synthesis of LSiPSCl

The reference sample (*i.e.*, S-LSiPSCl) was synthesised using the solid-state approach for comparison with the prepared L-LSiPSCl. The raw materials and target nominal compositions were the same as those used for the liquid-phase synthesis (*i.e.*, $Li_{10.02}Si_{1.47}P_{1.56}S_{11.7}Cl_{0.3}$). In this case, the raw materials were mixed using a planetary ball mill at a rotational speed of 380 rpm for 40 h, and the obtained precursor powder was sintered at 748 K for 8 h under a flow of Ar gas.

Sample characterisation

The elemental ratios of Li, Si, P, and S in the Li–P–S and Li–Si–S homogeneous solutions were determined by means of inductively coupled plasma atomic emission spectroscopy (ICP-AES, Vista-PRO, Varian Inc.). Phase identification for the synthesised powders was performed by X-ray diffraction (XRD) using a PANalytical X'Pert³ powder X-ray diffractometer with Cu Kα_1 (λ = 1.5406 Å) radiation. The diffraction data were collected with a step width of 0.03° over a 2θ range of 10–70° at 298 K. The particle morphologies of the fine-Li_2S and the synthesised samples were observed using field emission scanning electron microscopy (FE-SEM, Regulus 8230, Hitachi). The carbon present in the synthesised product was quantitatively analysed using the non-dispersive infrared method during combustion in a flow of oxygen (EMIA-810W, Horiba Ltd).

Electrochemical measurements

The alternating current impedance method was used to measure the ionic conductivities of the synthesised samples. Symmetric cells with Au powder electrodes on both surfaces of the sample pellets were prepared for the purpose of these measurements. More specifically, the sample pellets (diameter = 10 mm and thickness = 1–2 mm) were prepared at a relative density of approximately 70% under a pressure of 370 MPa. For measurements at 298 K, an amplitude of 50 mV was applied in the frequency range of 0.1 Hz to 1 MHz using a Solartron 1260 frequency response analyser. For the measurements at low temperatures between 220 and 190 K, an amplitude of 10 mV was applied in the frequency range of 20 Hz to 100 MHz using a Keysight E4990A frequency response analyser. The direct current (DC) polarisation measurements were performed at 298 K by applying a DC voltage of 0.5 V to the symmetric cells containing the Au powder electrodes, as

described above. An upper limit for the DC electronic conductivity was calculated from the stabilized current after 600 s.

Charge–discharge measurements were performed for the all-solid-state cells prepared using the synthesised samples as the solid electrolytes. Following the removal of large particles from the solid electrolyte powder using a sieve with a 10 μm mesh, the cathode composite was prepared by mixing the sieved powder (30 mg) with $LiCoO_2$ powder (70 mg, Toda Kogyo) coated with a 10 nm-thick layer of $LiNbO_3$ (MP-01, Powrex). The ratio of the cathode active material ($LiCoO_2$) in the cathode composite was adjusted to 70 wt%. As a separator, the solid electrolyte powder (80 mg) was pressed into a 10 mm diameter pellet. The cathode composite (5 mg), Al mesh, and an Al foil current collector were stacked on one side of the separator and pressed at a pressure of 550 MPa. Subsequently, an In–Li alloy anode consisting of lithium foil (thickness = 0.1 mm, diameter = 5 mm) and indium foil (thickness = 0.1 mm, diameter = 10 mm) was stacked on the opposite side of the separator along with a Cu mesh current collector and pressed at 220 MPa. Constant current charge–discharge tests were performed using a TOSCAT-3100 battery testing system (Toyo System, USA) at 298 K. The cut-off voltage was set at 1.9–3.6 V for the In–Li anode. The current density applied to the cell was 0.096 mA cm^{-2}, which corresponds to a 0.2 C rate.

Results and discussion

Optimisation of the synthetic conditions

ACN was selected as the solvent for our liquid-phase approach (see Fig. 1) due to the fact that it is a polar aprotic solvent that does not promote severe decomposition reactions in the raw materials and precursors. In addition, since ACN does not contain oxygen as a constituent element, it is not possible for the sulfur atoms present in the raw materials and precursors to undergo exchange reactions with oxygen.[19]

In terms of the solubilities of the various raw materials in ACN, LiCl is soluble without combination with the other raw materials,[20] while in the cases of Li_2S, SiS_2, and P_2S_5, it was necessary to prepare mixtures to promote their dissolution under the conditions employed in this study. More specifically, since it has been reported that P_2S_5 exhibits a high solubility in ACN at a molar ratio of 1 : 1 with Li_2S,[21] we dissolved a 1 : 1 molar ratio of Li_2S and P_2S_5 in ACN to obtain a homogeneous Li–P–S solution, wherein analysis by ICP-AES confirmed this stoichiometry; the concentrations of Li_2S and P_2S_5 in the homogeneous Li–P–S solution were approximately 10 wt%. We also found that SiS_2 was highly soluble in ACN when mixed with Li_2S in a molar ratio of 2 : 1, and this composition was confirmed by ICP-AES analysis, wherein the molar ratio of Si : Li in the homogeneous Li–Si–S solution was determined to be 1 : 1; the concentrations of SiS_2 and Li_2S in the homogeneous Li–Si–S solution were approximately 3.5 wt%.

Subsequently, the prepared Li–P–S and Li–Si–S solutions were combined to yield a homogeneous Li–Si–P–S solution. To synthesise samples with the target molar ratio, it was necessary to add powdered Li_2S to this homogeneous solution, since the achievable molar ratio between the Li_2S, P_2S_5, and SiS_2 components is limited due to the fact that they only exhibit high solubilities at specific molar ratios, as described above. More specifically, the homogeneous Li–Si–P–S solution contained a $Li_2S : P_2S_5 : SiS_2$ molar ratio of 2.1 : 1.1 : 2.0, indicating that the proportion of Li_2S was lower than that of the target molar ratio (*i.e.*, $Li_2S : P_2S_5 : SiS_2 = 6.6 : 1.1 : 2.0$ for LSiPSCl). Thus, to ensure a high reactivity for the added Li_2S powder, fine-Li_2S, which consists of fine particles measuring several hundred nanometres (see Fig. 2), was prepared and added to the homogeneous Li–Si–P–S solution to obtain the precursor slurry solution.

Unexpectedly, sulfur was volatilised with the solvent when the precursor slurry solution was dried at 453 K for 3 h under vacuum. Thus, to compensate for the amount of volatilised sulfur, excess sulfur was added to the precursor by dissolution of the homogenous Li–Si–S solution. To obtain the optimal conditions, precursor slurry solutions containing different amounts of excess sulfur were prepared to give the following molar ratios: $Li_2S : P_2S_5 : SiS_2 : LiCl : S = 6.6 : 1.1 : 2.0 : 0.4 : X$ (X = 0.0, 1.0, and 2.9). Precursor powders dried from precursor slurry solutions were composed of an amorphous phase and a small amount of Li_2S and β-Li_3PS_4, as indicated by XRD patterns in Fig. S2.† The sample sintered from each precursor powder was denoted as L-LSiPSCl-X (X = 0.0, 1.0, and 2.9), and the optimal molar ratio was determined in terms of the target material purity.

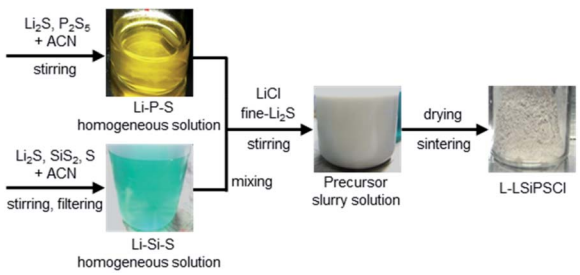

Fig. 1 Schematic representation of the liquid-phase process.

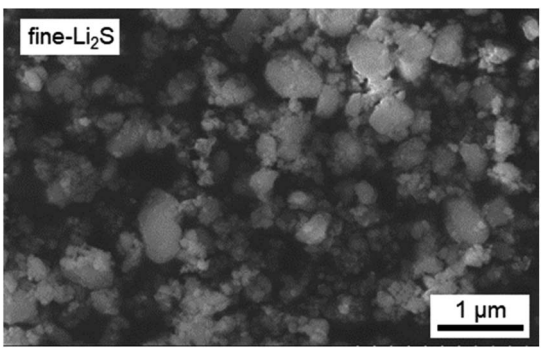

Fig. 2 SEM image of the fine-Li_2S particles.

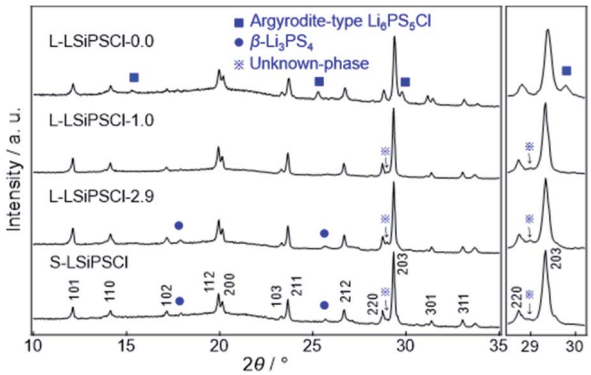

Fig. 3 XRD patterns of the L-LSiPSCl-X (X = 0.0, 1.0, and 2.9) and S-LSiPSCl samples.

Phase-conductivity relationship

Fig. 3 shows the XRD patterns recorded for the L-LSiPSCl-X (X = 0.0, 1.0, and 2.9) and S-LSiPSCl samples. It should be noted that the significant background modulation in each pattern was due to a Kapton film covering the sample during measurement. The main diffraction peaks were indexed to the same space group as the LGPS-type LSiPSCl (*i.e.*, $P4_2/nmc$, no. 137), thereby indicating that the target phase was formed as the main phase for all L-LSiPSCl samples. However, the L-LSiPSCl-0.0 (*i.e.*, without excess sulfur) sample also gave a peak corresponding to argyrodite-type Li_6PS_5Cl as a secondary phase,[22] while the impurity phase β-Li_3PS_4 was observed in the L-LSiPSCl-2.9 and S-LSiPSCl spectra. In contrast, only minor peaks from an unknown phase were observed in the spectrum of the L-LSiPSCl-1.0 sample.[23]

The lattice parameters of the main phase (*i.e.*, LGPS-type LSiPSCl) formed in the synthesised samples were then compared. More specifically, the peak positions close to 2θ = 29.5° were similar for the L-LSiPSCl-X (X = 1.0 and 2.9) and S-LSiPSCl samples, while that of the L-LSiPSCl-0.0 sample was observed at a higher angle. The unit cell volume determined from the Rietveld refinement was found to shrink by 0.69(3)% in the case of L-LSiPSCl-0.0 compared to those of L-LSiPSCl-X (X = 1.0 and 2.9) and S-LSiPSCl, and details are shown in Table S1.† This result indicates that the composition of the target LGPS-type phase in L-LSiPSCl-0.0 is slightly different from those of the L-LSiPSCl-X (X = 1.0 and 2.9) and S-LSiPSCl samples.

Subsequently, the impurity phases and the ionic conductivities were determined for the various samples, as summarised in Table 1. The conductivity for L-LSiPSCl-1.0 was 6.6 mS cm^{-1} at 298 K, which is higher than those obtained for the L-LSiPSCl-X (X = 0.0 and 2.9) samples. This difference was attributed to the formation of poorly conducting minor phases, such as the argyrodite-type Li_6PS_5Cl and β-Li_3PS_4 phases. In addition, the compositional difference in the main LGPS-type phase could also account for the reduced conductivity of L-LSiPSCl-0.0, as could the residual sulfur present in the L-LSiPSCl-2.9 sample.

Although L-LSiPSCl-1.0 showed the highest ionic conductivity among the samples prepared using our liquid-phase synthetic approach, its conductivity (6.6 mS cm^{-1}) was still lower than that of S-LSiPSCl (8.8 mS cm^{-1}). Since no significant differences were observed between the XRD patterns of these two products, we assumed that the decreased conductivity of L-LSiPSCl-1.0 originated from the grain boundary resistance rather than from any ionic resistance in the bulk crystalline phase. To verify this assumption, the total resistance was separated into its bulk and grain boundary components, and for each component, the impedance was measured in the high-frequency range up to 100 MHz and at low temperatures down to 190 K.

Thus, Fig. 4 shows the temperature dependences of the bulk and grain boundary resistance contributions of the L-LSiPSCl-1.0 and S-LSiPSCl samples; the resistance values presented in this figure were normalised according to the sample pellet dimensions. As a representative example, the Nyquist plot of L-LSiPSCl-1.0 at 190 K is shown in the inset, wherein two suppressed semicircles can be observed in the high and low frequency regions; the former was attributed to the bulk contribution and the latter to the grain boundary contribution. The obtained plots were fitted using the equivalent circuit

Table 1 Impurity phases and ionic conductivities (σ) at 298 K for the L-LSiPSCl-X (X = 0.0, 1.0, and 2.9) and S-LSiPSCl samples

Sample	σ/mS cm^{-1}	Impurity phases
L-LSiPSCl-0.0	3.5	Argyrodite-type Li_6PS_5Cl
L-LSiPSCl-1.0	6.6	Unknown phase
L-LSiPSCl-2.9	3.8	Unknown phase, β-Li_3PS_4
S-LSiPSCl	8.8	Unknown phase, β-Li_3PS_4

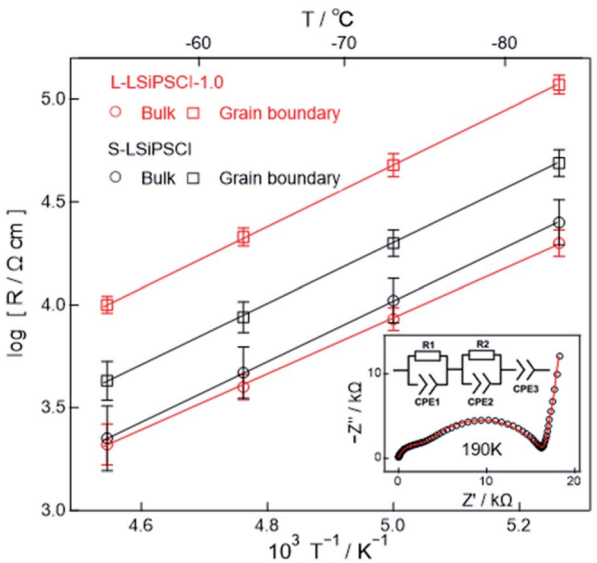

Fig. 4 Arrhenius plots of the bulk and grain boundary resistance components for the L-LSiPSCl-1.0 and S-LSiPSCl samples in the temperature range of 220–190 K. The inset shows the representative Nyquist plot for L-LSiPSCl-1.0 at 190 K and the equivalent circuit model used for fitting analysis; R1 and CPE1: bulk, R2 and CPE2: grain-boundary, and CPE3: electrode polarisation.

model (shown in the inset of Fig. 4), which comprises two parallel circuits of resistors (R1 and R2) and constant-phase elements (CPE1, CPE2, and CPE3) connected in series.[24] As a result, an Arrhenius plot was obtained for the bulk and grain boundary contributions in the low temperature range between 220 and 190 K. The bulk resistance, which is related to lithium ion conduction in the crystalline phase, was comparable for both L-LSiPSCl-1.0 and S-LSiPSCl. In contrast, the grain boundary resistance, which is related to the surface and the sample morphology, was higher for L-LSiPSCl-1.0 than for S-LSiPSCl. Therefore, the lower total conductivity for the former phase was concluded to be due to its higher grain-boundary resistance.

Inferring the origin of grain-boundary resistance in L-LSiPSCl

For pressed sulfide samples, such as those examined herein, it has been reported that the particle morphology can influence the ionic conductivity.[25] Thus, the particle morphologies of the L-LSiPSCl-1.0 and S-LSiPSCl samples were recorded by SEM at different magnifications. As can be seen from Fig. 5, the particle size distributions differed significantly between samples, ranging from 1 μm-diameter fine particles to >10 μm-diameter coarse particles. The SEM images obtained for L-LSiPSCl-1.0 (Fig. 5(a1) and (a2)) indicate that the coarse particles were aggregates composed of fine particles, while the S-LSiPSCl particles (Fig. 5(b1) and (b2)) were single particles. This observation suggests that the crystallites grew to a lesser degree in the case of L-LSiPSCl-1.0 than in the case of S-LSiPSCl. In addition, on the L-LSiPSCl-1.0 particle surface, large numbers of pores were visible, which were likely induced by the solvent volatilisation process.[26] From these SEM observations, it is therefore apparent that the L-LSiPSCl-1.0 sample possesses a greater number of particle interfaces and surface pores, which may act as obstacles for lithium ion conduction between the bulk crystalline particles, ultimately resulting in increased grain boundary resistance.

In addition to the particle morphology, the formation of a secondary phase with a low ionic conductivity was found to reduce the ionic conductivity of the sample, as observed for the L-LSiPSCl-X (X = 0.0 and 2.9) samples. In contrast, the L-LSiPSCl-1.0 and S-LSiPSCl samples contained significantly lower quantities of impurity phases, as discussed above. However, the chemical analyses suggested that carbonised species are formed on the L-LSiPSCl-1.0 particle surface from the residual solvent, which could not be fully removed by vacuum drying.[19,27] More specifically, the use of a non-dispersive infrared method to quantify the carbonised species showed that the carbon content for L-LSiPSCl-1.0 was 1.0 wt%, which is larger than that detected for S-LSiPSCl (*i.e.*, 0.5 wt%). The presence of carbonised species was also supported by micro-Raman spectroscopy, which indicated that the L-LSiPSCl-1.0 sample contained compounds with carbon-related chemical bonds (see Fig. S3†). The increased amount of carbides detected on the surface of the L-LSiPSCl-1.0 sample was therefore considered to partially account for its larger grain boundary resistance compared to S-LSiPSCl.

An all-solid-state cell

Although the presence of carbides could potentially increase the electronic conductivity of L-LSiPSCl-1.0, the DC polarisation measurements indicated that its electronic conductivity was of the same order as that of S-LSiPSCl. More specifically, the DC electronic conductivity was 8.9×10^{-6} mS cm^{-1} for L-LSiPSCl-1.0, which is slightly higher than that of S-LSiPSCl, but was nearly six orders of magnitude lower than the ionic conductivity, thereby indicating that L-LSiPSCl-1.0 is essentially a pure ionic conductor. Based on this promising result, the applicability of L-LSiPSCl-1.0 as a solid electrolyte in an all-solid-state battery was examined. Thus, Fig. 6 shows the charge–discharge curves of the all-solid-state cells prepared using L-LSiPSCl-1.0 or S-LSiPSCl as the solid electrolytes. More specifically, L-LSiPSCl-1.0 or S-LSiPSCl was used as the solid electrolyte in the separator, while the cathode composite was prepared by

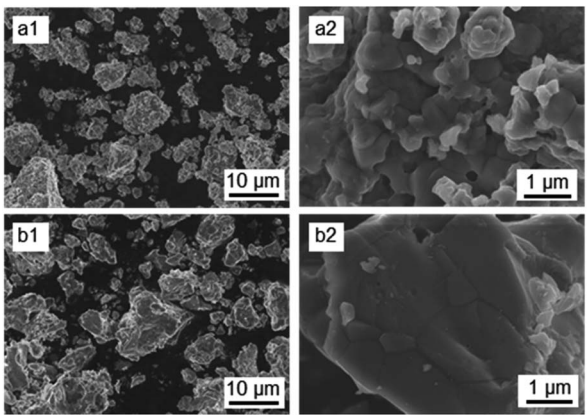

Fig. 5 SEM images of (a1 and a2) L-LSiPSCl-1.0 and (b1 and b2) S-LSiPSCl at different magnifications.

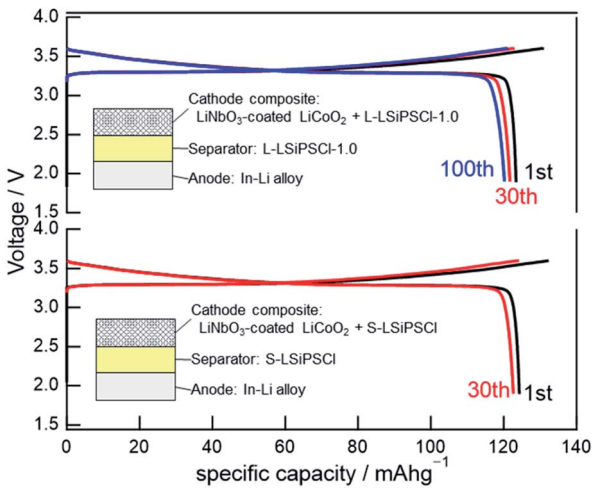

Fig. 6 Charge–discharge curves of the all-solid-state cells prepared using L-LSiPSCl-1.0 or S-LSiPSCl as the solid electrolyte. The current density applied to the cell was 0.096 mA cm^{-2}, which corresponds to a 0.2 C rate.

mixing L-LSiPSCl-1.0 or S-LSiPSCl with $LiNbO_3$-coated $LiCoO_2$, and an In–Li alloy was employed as the anode. As shown in Fig. 6, the all-solid-state cell based on L-LSiPSCl-1.0 exhibited an initial discharge capacity of 123 mA h g^{-1}, and this value dropped very slightly to 122 mA h g^{-1} for the 30th cycle; these values are comparable to those obtained for the cell based on S-LSiPSCl. The performance difference between the two cells was small, indicating that the performance of the all-solid-state cell was only slightly affected by the observed differences between L-LSiPSCl-1.0 and S-LSiPSCl, *i.e.*, the differences in the grain boundary resistance, the characteristic particle morphology, and the electronic conductivity. Importantly, the cell prepared using L-LSiPSCl-1.0 exhibited a discharge capacity of $\geq$120 mA h g^{-1} and a capacity retention of >97% during the 100th cycle, thereby implying that L-LSiPSCl-1.0 functions as a stable solid electrolyte in the separator and cathode composite.

Conclusions

We herein report the development of a liquid-phase synthetic route for the preparation of the $Li_{10}GeP_2S_{12}$ (LGPS)-type phase in the Li–Si–P–S–Cl system (LSiPSCl). In this liquid-phase synthesis, the phase purity and ionic conductivity of the samples were optimised by adjusting the sulfur ratio in the precursor slurry solution. Among the samples synthesised *via* the liquid-phase process (denoted as L-LSiPSCl), the L-LSiPSCl-1.0 phase, which was obtained from the precursor with a $Li_2S : P_2S_5 : SiS_2 : LiCl : S$ molar ratio of 6.6 : 1.1 : 2.0 : 0.4 : X (X = 1.0), exhibited the highest phase purity, in addition to the highest ionic conductivity of 6.6 mS cm^{-1} at 298 K. Compared with the sample synthesised according to the conventional solid-state approach (denoted as S-LSiPSCl), the grain-boundary resistance contribution at 190 K was 2.4 times larger for L-LSiPSCl-1.0 than for S-LSiPSCl. In addition, in the case of the L-LSiPSCl-1.0 sample, scanning electron microscopy observations indicated a characteristic particle morphology with a large number of particle interfaces and surface pores, while the presence of carbides was confirmed by both micro-Raman spectroscopy and a non-dispersive infrared method. These features of L-LSiPSCl-1.0 accounted for the larger grain boundary resistance of this sample compared to that of S-LSiPSCl. Subsequently, all-solid-state cells were prepared using either L-LSiPSCl-1.0 or S-LSiPSCl as the solid electrolyte. A mixture of either L-LSiPSCl-1.0 or S-LSiPSCl with $LiNbO_3$-coated $LiCoO_2$ produced the composite cathode, while an In–Li alloy was used as the anode. The discharge capacity for the cell prepared using L-LSiPSCl-1.0 was 88% of its theoretical value after 100 cycles (*i.e.*, 137 mA h g^{-1} for 1.9–3.6 V *vs.* Li^+/In–Li), and its capacity retention was >97%. Importantly, this solid electrolyte demonstrated high cycle stability, which was comparable to that of the cell prepared using S-LSiPSCl, thereby indicating the potential of the liquid-phase preparation process to replace the conventional solid-state process to generate such solid electrolytes. Moreover, the applicability of L-LSiPSCl-1.0 in all-solid-state cells was also confirmed. Overall, our results suggest that the described liquid-phase approach could potentially be employed for the large-scale production of lithium superionic conductors, including LGPS-type solid electrolytes.

Author contributions

The manuscript was written through contributions from all authors. All authors discussed the results, contributed to the manuscript writing, and approved its final version.

Conflicts of interest

There are no conflicts to declare.

Acknowledgements

This research was partly supported by the Program on Open Innovation Platform with Enterprises, Research Institute and Academia (OPERA) [JPMJOP1862] from the Japan Science and Technology Agency (JST).

References

1 Q. Wang, L. Jiang, Y. Yu and J. Sun, *Nano Energy*, 2019, **55**, 93–114.
2 A. Manthiram, X. Yu and S. Wang, *Nat. Rev. Mater.*, 2017, **2**, 16103.
3 Y. Kato, K. Kawamoto, R. Kanno and M. Hirayama, *Electrochemistry*, 2012, **80**, 749–751.
4 Y. Kato, S. Shiotani, K. Morita, K. Suzuki, M. Hirayama and R. Kanno, *J. Phys. Chem. Lett.*, 2018, **9**, 607–613.
5 N. Kamaya, K. Homma, Y. Yamakawa, M. Hirayama, R. Kanno, M. Yonemura, T. Kamiyama, Y. Kato, S. Hama, K. Kawamoto and A. Mitsui, *Nat. Mater.*, 2011, **10**, 682–686.
6 Y. Kato, S. Hori, T. Saito, K. Suzuki, M. Hirayama, A. Mitsui, M. Yonemura, H. Iba and R. Kanno, *Nat. Energy*, 2016, **1**, 16030.
7 S. Hori, K. Suzuki, M. Hirayama, Y. Kato and R. Kanno, *Front. Energy Res.*, 2016, **4**, 38.
8 Y. Sun, K. Suzuki, K. Hara, S. Hori, T. Yano, M. Hara, M. Hirayama and R. Kanno, *J. Power Sources*, 2016, **324**, 798–803.
9 K. Suzuki, M. Sakuma, S. Hori, T. Nakazawa, M. Nagao, M. Yonemura, M. Hirayama and R. Kanno, *Solid State Ionics*, 2016, **288**, 229–234.
10 J. Liang, N. Chen, X. Li, X. Li, K. R. Adair, J. Li, C. Wang, C. Yu, M. Norouzi Banis, L. Zhang, S. Zhao, S. Lu, H. Huang, R. Li, Y. Huang and X. Sun, *Chem. Mater.*, 2020, **32**, 2664–2672.
11 L. Ye, E. Gil-González and X. Li, *Electrochem. Commun.*, 2021, **128**, 107058.
12 A. Miura, N. C. Rosero-Navarro, A. Sakuda, K. Tadanaga, N. H. H. Phuc, A. Matsuda, N. Machida, A. Hayashi and M. Tatsumisago, *Nat. Rev. Chem.*, 2019, **3**, 189–198.
13 Z. Liu, W. Fu, E. A. Payzant, X. Yu, Z. Wu, N. J. Dudney, J. Kiggans, K. Hong, A. J. Rondinone and C. Liang, *J. Am. Chem. Soc.*, 2013, **135**, 975–978.

14 S. Teragawa, K. Aso, K. Tadanaga, A. Hayashi and M. Tatsumisago, *J. Mater. Chem. A*, 2014, **2**, 5095–5099.
15 M. Calpa, N. C. Rosero-Navarro, A. Miura and K. Tadanaga, *RSC Adv.*, 2017, **7**, 46499–46504.
16 Y. Wang, Z. Liu, X. Zhu, Y. Tang and F. Huang, *J. Power Sources*, 2013, **224**, 225–229.
17 K. Suzuki, A. Yageta, Y. Ikeda, N. Mashimo, S. Hori, M. Hirayama and R. Kanno, *Chem. Lett.*, 2020, **49**, 1379–1381.
18 Y. Higashiyama, T. Nakagawa and N. Machida, *J. Jpn. Soc. Powder Powder Metall.*, 2022, **69**, 117–120.
19 A.-K. Hatz, R. Calaminus, J. Feijoo, F. Treber, J. Blahusch, T. Lenz, M. Reichel, K. Karaghiosoff, N. M. Vargas-Barbosa and B. V. Lotsch, *ACS Appl. Energy Mater.*, 2021, **4**, 9932–9943.
20 N. Xin, Y. Sun, M. He, C. J. Radke and J. M. Prausnitz, *Fluid Phase Equilib.*, 2018, **461**, 1–7.
21 M. Calpa, N. C. Rosero-Navarro, A. Miura, K. Terai, F. Utsuno and K. Tadanaga, *Chem. Mater.*, 2020, **32**, 9627–9632.
22 M. A. Kraft, S. P. Culver, M. Calderon, F. Bocher, T. Krauskopf, A. Senyshyn, C. Dietrich, A. Zevalkink, J. Janek and W. G. Zeier, *J. Am. Chem. Soc.*, 2017, **139**, 10909–10918.
23 Y. Li, S. Daikuhara, S. Hori, X. Sun, K. Suzuki, M. Hirayama and R. Kanno, *Chem. Mater.*, 2020, **32**, 8860–8867.
24 P. Braun, C. Uhlmann, A. Weber, H. Störmer, D. Gerthsen and E. Ivers-Tiffée, *J. Electroceram.*, 2017, **38**, 157–167.
25 S. Yubuchi, M. Uematsu, C. Hotehama, A. Sakuda, A. Hayashi and M. Tatsumisago, *J. Mater. Chem. A*, 2019, **7**, 558–566.
26 H. Wang, Z. D. Hood, Y. Xia and C. Liang, *J. Mater. Chem. A*, 2016, **4**, 8091–8096.
27 S. Yubuchi, M. Uematsu, M. Deguchi, A. Hayashi and M. Tatsumisago, *ACS Appl. Energy Mater.*, 2018, **1**, 3622–3629.

